



Creep Rupture Performance of Welds of P91 Pipe Steel

A strong effect of Al content on creep resistance was observed and explained based on weld metal microstructure and precipitation thermodynamics/kinetics

BY X. CHAI, J. C. BUNDY, M. A. AMATA, C. ZHANG, F. ZHANG, S. CHEN, S. S. BABU, AND S. KOU

ABSTRACT

The creep resistance of welds of P91 pipe steel was investigated, focusing on the effect of the Al content in the fusion zone. Two welds were made with significantly different Al contents, one high at 0.455 wt-% and the other low at 0.001 wt-%. The N contents were comparable, 0.035 wt-% in the high-Al weld and 0.043 wt-% in the low-Al one. After postweld heat treatment at 760°C for 4 h, specimens were prepared from inside the fusion zones for creep rupture tests. The high-Al weld showed a much lower creep resistance than the low-Al one. To explain the significant effect of Al on the creep resistance, the microstructure of the welds, especially retained δ -ferrite and nitride precipitates, was examined by optical and electron microscopy and discussed based on either existing data or calculated results of thermodynamics and kinetics. First, the presence or absence of retained δ -ferrite in the martensite matrix was checked and discussed in light of Al as a strong ferrite stabilizer. Second, precipitates in the welds were examined by electron microscopy, including their sizes and compositions, especially the contents of Al, Cr, and V. Third, the formation of the precipitates of AlN, VN, and NbN was further discussed based on the Ellingham diagram, data of the solubility products, and the volume fractions of AlN, VN, and NbN calculated using the thermodynamic software package Pandat.

KEYWORDS

• Creep Resistance • P91 • Aluminum Content • Ferritic Steels • Pipe

Introduction

P91 steel, a modified 9Cr-1Mo steel for use as pipes, is one of the new 9–12% Cr ferritic martensite steels designed to improve creep resistance. P91 steel contains vanadium (V), niobium (Nb), and nitrogen (N) as minor alloying elements to improve the creep resistance by fine precipitates of vanadium carbonitride V(CN) and niobium

carbonitride Nb(CN) in a tempered martensite matrix (Refs. 1–9). These precipitates are commonly denoted as MX precipitates, where M stands for V or Nb and X for carbon and/or nitrogen. Regardless of MX, $M_{23}C_6$ carbide precipitates from the martensitic matrix, where M denotes Cr and Fe and C for carbon. In comparison to MX precipitates, $M_{23}C_6$ precipitates are much less stable morphologically at elevated

temperatures. At elevated temperatures, they tend to coarsen over time much more significantly than MX precipitates and are thus less able to resist creep by pinning down the movements of dislocations and interfaces, such as prior austenite grain boundaries, prior martensite lath boundaries, and subgrain boundaries (Refs. 5, 10–17). It has been suggested (Ref. 11) that subgrain boundary migration may control the recovery of dislocations and that subgrain boundary hardening enhanced by fine dispersions of precipitates along the internal interfaces is one of the most important strengthening mechanisms in 9–12%Cr ferritic steels (Ref. 12). It is worth noting that David et al. (Ref. 9) and Siefert and David (Ref. 18) have reviewed the weldability of new alloys developed for advanced fossil power plants including ferritic and austenitic alloys.

The production of P91 steel usually involves normalization at about 1050°C, air cooling to the room temperature to form martensite, and then reheating at about 750°C to temper the martensite (Ref. 19). The evolution of the type and size distribution of precipitates during the above preweld tempering condition also controls the Type IV creep failure observed in the heat-affected zone (HAZ) (Refs. 9, 20, 21). The present study pertains to the microstructure evolution in the fusion zone.

X. CHAI and S. KOU are, respectively, graduate student and professor at the Department of Materials Science and Engineering, the University of Wisconsin, Madison, Wis. J. C. BUNDY and M. A. AMATA are with Hobart Brothers, Troy, Ohio. C. ZHANG, F. ZHANG, and S. CHEN are with CompuTherm LLC, Madison, Wis. S. S. BABU is with the Department of Mechanical, Aerospace, and Biomedical Engineering, the University of Tennessee, Knoxville, Tenn.

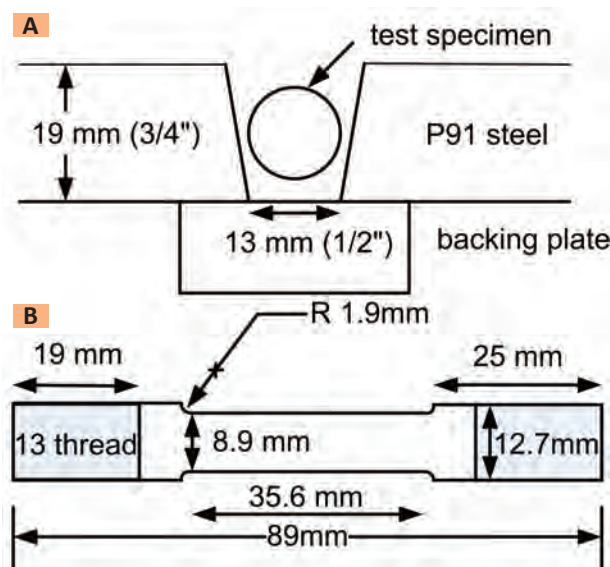


Fig. 1 — Designs for welding and creep-rupture testing. A — Joint design for butt-joint welding; B — creep-rupture test specimen.

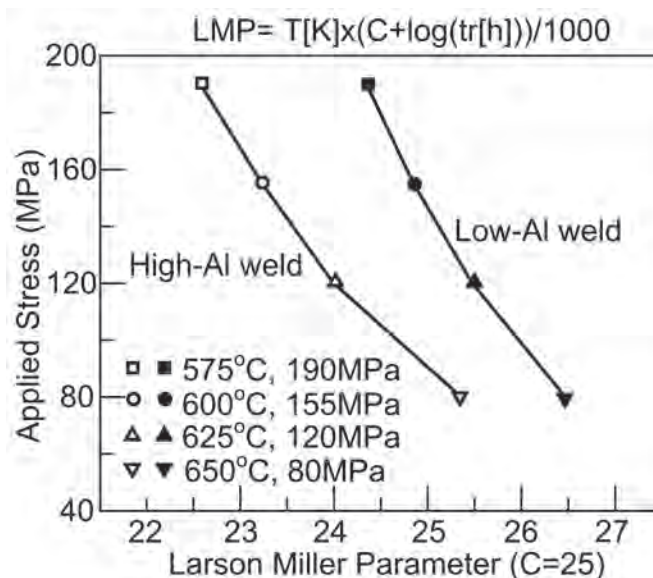


Fig. 2 — Results of creep-rupture tests (Table 3) showing much lower creep resistance of high-Al weld by plotting applied stress vs. Larson-Miller parameter (LMP), where $T[K]$ is temperature in degrees Kelvin and $tr[h]$ is time to rupture in hours.

-ferrite is the first solid phase to form during solidification, that is, the primary solidification phase, and it transforms to austenite upon further cooling. However, the γ transformation may not be complete in many alloy compositions. This phenomenon had been observed in self-shielded flux cored arc welds containing high concentration (1.8 wt-%) of aluminum (Al) (Ref. 22).

This can also be seen from the study of Mayr et al. (Ref. 23) on a 9-Cr steel similar to P91 by in-situ X-ray diffraction using synchrotron radiation. They showed that γ -ferrite is nucleated upon heating (at 10 K/s) the steel to 1210°C (1483 K) and the amount of γ -ferrite was 19% upon further heating into the γ region to the peak temperature of 1300°C (1573 K). Upon cooling, the γ -ferrite transformed back to austenite but the transformation was incomplete, resulting in about 2% retained γ -ferrite when the martensite transformation started. Thus, it is likely in welding P91 steel to find retained γ -ferrite in the martensite matrix in the fusion

zone as a result of cooling during solidification and in the HAZ as a result of cooling after reheating into the γ region.

The presence of γ -ferrite in the fusion zone of P91 steel has been reported (Ref. 24). The γ -ferrite tends to be elongated during creep rupture test near the fracture surface (Ref. 3). Since γ -ferrite is much softer than the surrounding martensite matrix, it can reduce the creep resistance of the fusion zone significantly (Refs. 9, 25).

For power plant applications, the weld metal, beside good creep resistance, needs to have adequate toughness to meet pressure test and other requirements at the room temperature, e.g., to withstand transient stresses during shutdown periods, as pointed out by Arivazhagan et al. (Ref. 6), Sireesha et al. (Ref. 7), and Francis et al. (Ref. 8). Arivazhagan et al. (Ref. 6) and Sireesha et al. (Ref. 7) suggested that reduction in Nb, N, and Si contents improves toughness, but the Ni content has to be adjusted such that the lower critical temperature (A_{C1}) temperature does not fall below the

postweld heat treatment (PWHT) temperature. The need to balance filler material composition to restrict the occurrence of γ -ferrite and ensure a fully martensitic structure in the fusion zone has also been emphasized (Refs. 9, 25).

The effect of Al on the creep resistance of welds of P91 steel has not been investigated so far. An experimental study unrelated to welding was conducted by Naoi et al. (Ref. 26) on 9Cr-0.5Mo-1.8W steel, which is somewhat similar to P91 steel. They observed that increasing the Al content improved the toughness of 9Cr-0.5Mo-1.8W steel at the room temperature. This improvement was attributed to grain refining caused by Al nitride precipitates. However, they also reported that the Al addition reduced the creep resistance. A computational study unrelated to welding was conducted by Magnusson et al. (Ref. 27). Their calculations showed that the Al additions to P91 steel could reduce the creep rupture life by a factor of six.

The present study was conducted to

Table 1 — Nominal Composition of P91 Steel (Ref. 29)

| Element | C | Mn | P | S | Si | Cr | Mo | V | Nb | N | Al | Ni |
|----------|------|------|-------|-------|------|------|------|------|------|-------|------|------|
| Min wt-% | 0.08 | 0.30 | — | — | 0.20 | 8.00 | 0.85 | 0.18 | 0.06 | 0.030 | — | — |
| Max wt-% | 0.12 | 0.60 | 0.020 | 0.010 | 0.50 | 9.50 | 1.05 | 0.25 | 0.1 | 0.070 | 0.04 | 0.40 |

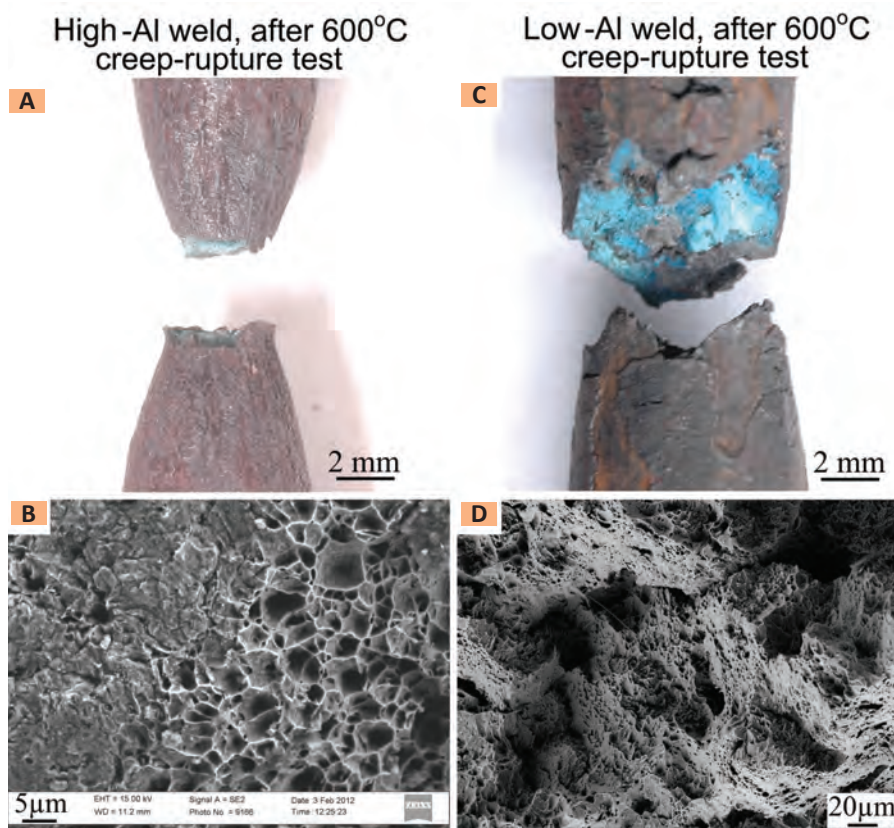


Fig. 3 — Weld specimens after creep rupture tests at 600°C. A, C — Macrographs showing much more necking with high-Al weld; B, D — SEM images of fractured surfaces showing clear microvoids characteristic of ductile fracture with high-Al weld.

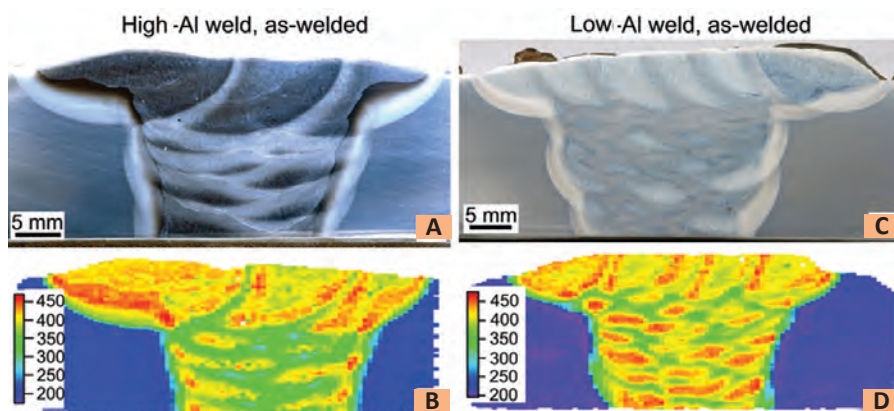


Fig. 4 — Transverse macrographs and hardness distributions in high- and low-Al welds in as-welded condition. A, C — Transverse macrographs; B, D — microhardness maps.

investigate the effect of Al on the creep resistance of the welds (the fusion zone) of P91 steel. The addition of Al to the welding consumable for P91 steel is intended to significantly lower the oxygen content in the weld metal, which is known to enhance the toughness of steel welds (Ref. 28). It is essential to know how the Al addition affects the

creep resistance of the weld metal.

Experimental Procedure

The nominal composition of P91 steel is shown in Table 1 (Ref. 29). P91 steel is for fabrication of pipes. A large plate, e.g., 19 mm ($\frac{3}{4}$ in.) in thickness, can be bent and welded along the lon-

Table 2 — Measured Composition of welds

| Element | High-Al Weld wt-% | Low-Al Weld wt-% |
|---------|----------------------|---------------------|
| C | 0.114±0.004 | 0.117±0.008 |
| Mn | 1.025±0.025 | 0.55±0.01 |
| P | 0.007±0.001 | 0.013 |
| S | 0.004 | 0.009±0.001 |
| Si | 0.11±0.01 | 0.34±0.01 |
| Cr | 8.09±0.2 | 8.22 |
| Mo | 0.865±0.065 | 1.06±0.01 |
| V | 0.165±0.005 | 0.28±0.01 |
| Nb | 0.047±0.004 | 0.051±0.001 |
| Al | 0.455±0.035 | 0.001 |
| N | 0.035±0.001 | 0.043±0.001 |
| O | 0.028±0.003 | 0.1±0.005 |
| Ni | 0.04 | 0.72±0.01 |
| Cu | 0.04 | 0.04 |

gitudinal joint to make a pipe, and the specimens for creep rupture tests can be prepared from the weld metal inside the fusion zone. However, in order to follow AWS A5.29/A5.29M: 2010, *Specification for Low-Alloy Steel Electrodes for Flux Cored Arc Welding* (Ref. 30), the butt joint design in Fig. 1A (which is consistent with Fig. 3 in the AWS specification) was used. A root opening was provided between the two plates to allow multipass welding with the use of a filler metal. A piece of P91 steel 13 mm ($\frac{1}{2}$ in.) in thickness and 32 mm ($1\frac{1}{4}$ in.) in width was used as a backing plate.

Two welding consumables were used to weld P91 steel. One was a commercially available covered electrode, E9015-B9 H4R, for shielded metal arc welding (SMAW), and the other was an experimental tubular electrode for flux cored arc welding (FCAW). Shielded metal arc welding was conducted with an average current of 140 A, an average voltage of 22.5 V, and a welding speed of 2.88 mm/s (6.8 in./min) in 33 passes, and the linear heat input was calculated as 1.09 kJ/mm (27.8 kJ/in.). Flux cored arc welding, on the other hand, was conducted with a mixture of Ar and CO₂ for shielding and with an average current of 260 A, an average voltage of 27 V and a travel speed of 4.23 mm/s (10 in./min) in 13 passes, the linear heat input can be calculated as 1.66 kJ/mm (42.2 kJ/in.). The preheat and interpass temperatures were 260°C (500°F) for both welding processes. The fewer passes in FCAW were because the electrode was designed for welding with a relatively high welding current. Differences in the thermal cycles due to heat input

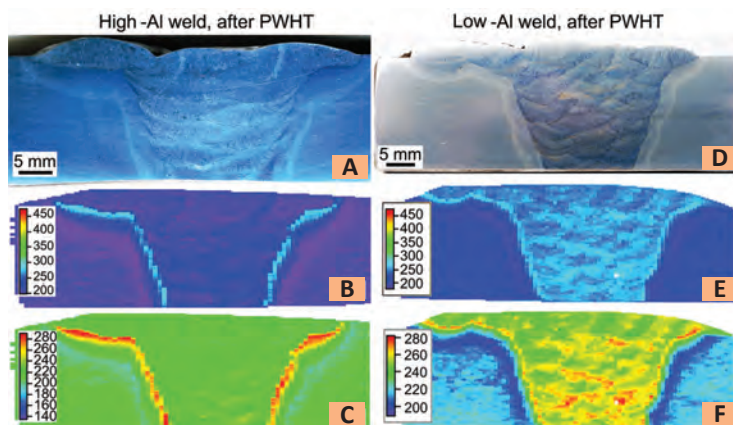


Fig. 5 — Hardness maps on welds after postweld heat treatment showing lower hardness in fusion zone of the high-Al weld than that of the low-Al weld. A, D — Transverse macrographs; B, E — microhardness maps; C, F — hardness scale changed.

are likely to affect the weld metal precipitation, but the large differences in chemical composition are expected to overshadow the effect of different heat inputs. Chemical analysis was performed on “undiluted” weld metal. Most element determinations were made using optical emission spectroscopy (Bruker-Quantron Q8 Magellan). Nitrogen and oxygen were determined using the fusion method (LECO TC-436), and carbon was determined using the combustion method with a LECO CS-200 instrument.

Microhardness measurements were conducted on weld specimens in the as-welded condition and after PWHT at 760°C (1400°F) for 4 h, which is in the suggested PWHT temperature range (730° to 770°C) for P91 steel welds by David et al. (Refs. 9, 18). Sireesha et al. (Ref. 7) also found PWHT at 760°C significantly improved the fusion zone toughness and Silwal et al. (Ref. 31) found PWHT at the same temperature significantly improved the HAZ toughness. Microhardness measurements were conducted automatically using a LECO AMH-43 system with computer-controlled scanning of the weld specimen (Ref. 32). Additional microhardness indentations were made manually at selected locations in the welds with a Tukon 1102/1202 Knoop/Vickers automated hardness tester from Wilson Hardness.

After PWHT, specimens for creep rupture tests were prepared according to the design shown schematically in Fig. 1B. Essentially, rods 13 mm (0.5 in.) in diameter and 89 mm (3.5 in.) long

were machined from the fusion zone in the longitudinal direction such that the rod axis was along the centerline of the fusion zone. The mid-section of the rod was reduced by machining to provide a 35.6-mm gauge length of 8.9 mm diameter. Threads were provided at the two ends of the rod to allow connection to the fixtures of the test machine.

Creep rupture tests were conducted in air in standard creep rupture frames at AMC Vulcan Laboratories of Birmingham, Ala. The tests ranged from 190 MPa (27.6 ksi) at 575°C to 80 MPa (11.6 ksi) at 650°C and lasted up to 5000 h. These ranges were selected based on the expected service temperatures and the stress levels estimated for rupture to occur in one thousand hours in the base metal. The yield stress of P91 steel, either the base metal or the weld metal, is over 300 MPa at 575°C and 200 MPa at 650°C (Ref. 33). These are well above the 190 MPa stress level applied in the creep rupture test at 575°C and the 80 MPa stress level at 650°C.

Results and Discussion

The chemical composition of the high-Al weld made by FCAW is shown in Table 2. The 8.09 wt-% Cr and 0.865 wt-% Mo are close to the nominal composition of 8.75 wt-% Cr and 0.95 wt-% Mo of P91 steel (Table 1). The C,

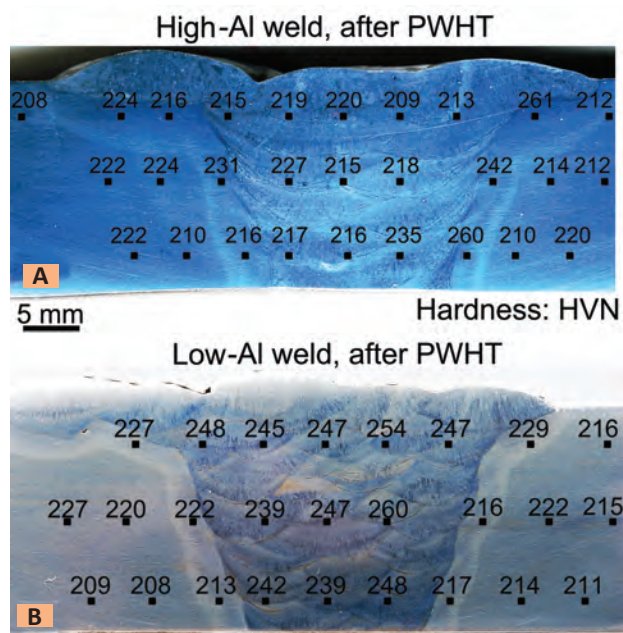


Fig. 6 — Hardness measurements after postweld heat treatment showing lower hardness in the high-Al weld than in the low-Al weld. A — High-Al weld with an average hardness of 219 HV in fusion zone; B — low-Al weld with an average hardness of 247 HV in fusion zone.

V, and Nb contents were 0.114, 0.165, and 0.047 wt-%, respectively. In addition, the weld contained 0.455 wt-% Al and 0.035 wt-% N.

The chemical composition of the low-Al weld made by SMAW is also shown in Table 2. The fusion zone contained 8.22 wt-% Cr and 1.06 wt-% Mo, again close to the nominal Cr and Mo contents of P91 steel, respectively (Table 1). The C, V, and Nb contents were 0.117, 0.28, and 0.051 wt-%, respectively. The N content was 0.043 wt-%, comparable to that of 0.035 wt-% in the high-Al weld made by FCAW. However, unlike the high-Al weld, it was nearly Al free (0.001 wt-% Al).

Creep Rupture Tests

Table 3 shows the results of creep rupture tests of the high- and low-Al welds. As shown, the high-Al weld lasted much shorter in creep rupture tests before failure, up to about 300 h as compared to about 5000 h for the low-Al welds. This difference is consistent with the adverse effect of Al on the creep resistance of P91 steel (Ref. 27) and 9Cr-0.5Mo-1.8W steel (Ref. 26) reported in previous studies unrelated

to welding.

In Fig. 2, the applied stress is plotted vs. the Larson Miller Parameter (LMP) defined as follows:

$$LMP = \frac{T[K] \times (C + \log(\text{tr}[h]))}{1000} \quad (1)$$

where $T[K]$ is temperature in degrees Kelvin, C is a constant taken as 25, and $\text{tr}[h]$ is time to rupture in hours.

As expected, the curve for the high-Al weld is significantly more to the left, indicating its much lower resistance to creep rupture as compared to the low-Al weld.

Considerable necking occurred before rupture in all the high-Al weld specimens down to 80 MPa. Figure 3A shows necking in the specimen tested at 600°C and 155 MPa, which is consistent with the low creep resistance of this specimen, that is, significant deformation under tensile loading at the test temperature. According to Table 3, this specimen had a 51.4% elongation and 87.1% reduction in cross-sectional area. The SEM image of the fracture surface in Fig. 3B reveals clear dimples and hence the ductile nature of failure, again consistent with the low creep resistance of the specimen.

Only slight necking occurred in the low-Al weld under identical test conditions as can be seen in Fig. 3C, which is consistent with the high creep resistance of the specimen. According to Table 3, this specimen had a 13% elongation and 29.1% reduction in cross-sectional area. The SEM images of the fracture surface in Fig. 3D reveal no clear dimples like those typical of ductile failure (Fig. 3B), again consistent with the high creep resistance of the specimen.

Hardness Distributions

Figure 4A shows the transverse cross section of the high-Al weld in the as-welded condition. Due to the multipass nature of the weld, the microstructure in the fusion zone is not uniform. Figure 4B shows the hardness distribution in the weld, which is not uniform, either. The HAZ of a pass can be well inside the fusion zone and HAZ of its previous pass. This can cause local reheating and hence microstructural and hardness changes within the fusion zone (Refs. 9, 34).

As can be seen from the last pass

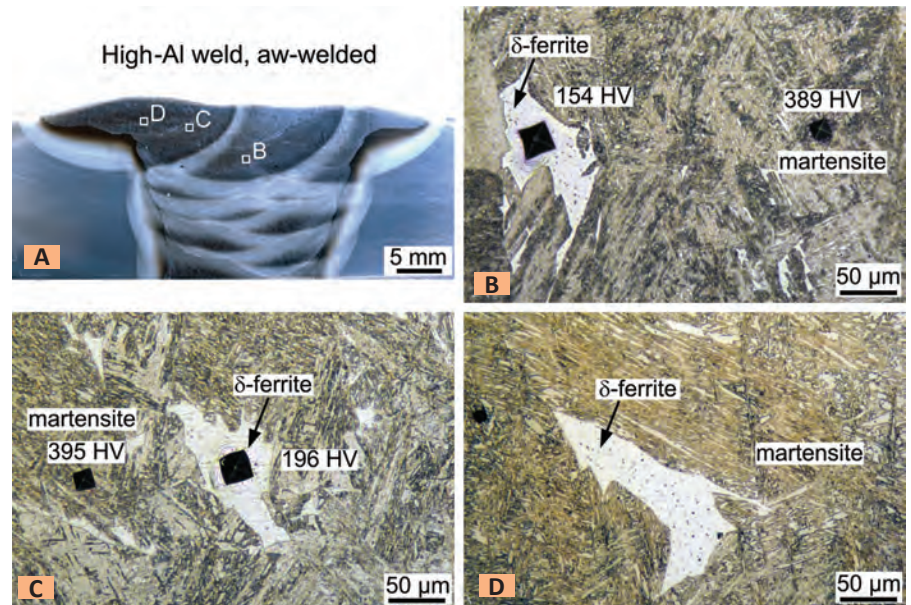


Fig. 7 — Presence of soft δ -ferrite in harder matrix of martensite in high-Al weld in as-welded condition. A — Transverse macrograph of weld; B — optical micrograph at point B in A; C — at point C; D — at point D.

Table 3 — Results of Creep Rupture Tests of the High-Al Weld and the Low-Al Weld

| Weld | Temperature (°C) | Stress (MPa) | Rupture (h) | % Elong | % RA |
|--------------|------------------|--------------|-------------|---------|------|
| High-Al weld | 575 (1067°F) | 190 | 41.4 | 35.6 | 82.0 |
| Low-Al weld | 575 (1067°F) | 190 | 5110 | 11.3 | 30.6 |
| High-Al weld | 600 (1112°F) | 155 | 41.1 | 51.4 | 87.1 |
| Low-Al weld | 600 (1112°F) | 155 | 2875.2 | 13.0 | 29.1 |
| High-Al weld | 625 (1157°F) | 120 | 52.2 | 43.8 | 82.5 |
| Low-Al weld | 625 (1157°F) | 120 | 2326.0 | 12.9 | 33.2 |
| High-Al weld | 650 (1202°F) | 80 | 296.4 | 42.6 | 59.8 |
| Low-Al weld | 650 (1202°F) | 80 | 4713.6 | 13.5 | 36.1 |

shown in Fig. 4B, the maximum hardness is about 475 HV and is immediately along the fusion boundary, that is, the coarse-grained HAZ (CGHAZ). This is reasonably close to the average hardness of about 510 HV observed by Silwal et al. (Ref. 31) in the CGHAZ of P91 steel in the as-welded condition. According to them, the CGHAZ experienced during welding a peak temperature between 1100°C (above the A_{C3} temperature 925°C) and the melting temperature of 1382°C, thus allowing complete carbide dissolution and austenite grain growth and hence formation of brittle martensite upon cooling.

Figure 4C shows the transverse

cross section of the low-Al weld in the as-welded condition. As compared to the high-Al weld (Fig. 4A), the low-Al weld has a more uniform microstructure due to the more and smaller passes used (33 vs. 13). The microhardness distribution in the fusion zone, as shown in Fig. 4D, is also more uniform than that of the high-Al weld (Fig. 4B).

Figure 5A shows the transverse cross section of the high-Al weld after PWHT at 760°C (1400°F) for 4 h. As compared to the as-welded condition (Fig. 4A), the microstructure in the fusion zone is more uniform. Consequently, the microhardness in the fusion zone is also more uniform as can be seen in Fig. 5B. On the average, the

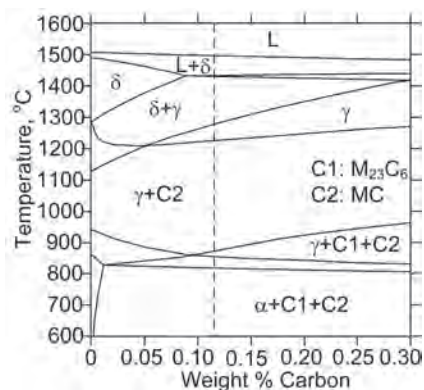


Fig. 8 — Quasi-binary phase diagram of T91 steel (Ref. 36) shown here to illustrate formation of δ -ferrite in fusion zone during solidification and in HAZ during reheating by subsequent passes to near 1300°C. Incomplete transformation of the δ -ferrite to austenite γ upon cooling causes retained δ -ferrite.

hardness is significantly lower after postweld heat treatment. For better resolution of the hardness distribution, a different color scale for hardness was used in Fig. 5C. As can be seen from the last pass shown in Fig. 5C, the maximum hardness is about 290 HV and is again in the CGHAZ immediately along the fusion boundary. The PWHT at 760°C for 4 h did not make the CGHAZ identical to the base metal in hardness, but it still reduced the CGHAZ hardness significantly (from about 475 to 290 HV). Silwal et al. (Ref. 31) reduced the hardness in the CGHAZ of P91 steel from about 510 to 290 HV after PWHT at 800°C for 2 h.

Figure 5D shows the transverse cross section of the low-Al weld after PWHT at 760°C (1400°F) for 4 h. The microstructure in the fusion zone is more uniform than that in the as-welded condition — Fig. 4C. The microhardness in the fusion zone is shown in Fig. 5E, which is also more uniform and, on the average, significantly lower than that in the as-welded condition — Fig. 4D. In Fig. 5F, a different color scale for hardness is used to show the hardness distribution.

In order to determine the average hardness in the fusion zone, additional microhardness measurements were conducted manually in the weld specimens after PWHT, and the results are shown in Fig. 6. For the high-Al weld,

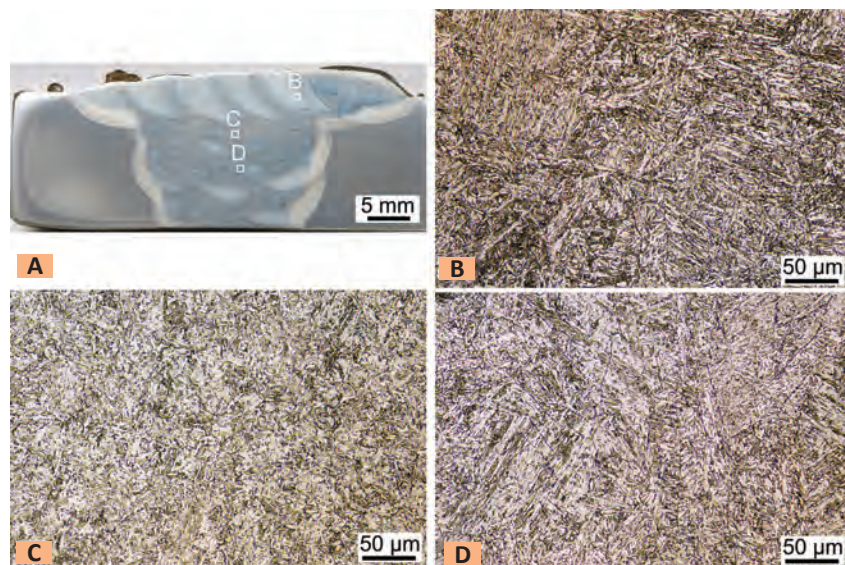


Fig. 9 — Absence of δ -ferrite in low-Al weld in as-welded condition. A — Transverse macrograph of weld; B — optical micrograph at point B in A; C — at point C; D — at point D.

Table 4 — Solubility Products^(a) for Carbides and Nitrides in Steels (Ref. 40)

| Compound | Metal | Nonmetal | A | B |
|----------------------------|-------|-------------------|----------------|-------|
| Cr_{23}C_6 | Cr | C | 5.90 | 7375 |
| V_4C_3 | V | $\text{C}_{0.75}$ | 5.36 | 8000 |
| TiC | Ti | C | 2.75 | 7000 |
| NbC | Nb | $\text{C}_{0.7}$ | 3.11 | 7520 |
| Mo_2C | Mo | C | 5.0 | 7375 |
| Nb(C,N) | Nb | (CN) | 2.26 | 6700 |
| VN | V | N | 2.27 | 7070 |
| VN | V | N | 3.46 + 0.12%Mn | 8330 |
| AlN | Al | N | 1.80 | 7750 |
| AlN | Al | N | 1.03 | 6770 |
| NbN | Nb | N | 4.04 | 10230 |
| NbN | Nb | N | 3.70 | 10800 |
| TiN | Ti | N | 0.32 | 8000 |

(a) The data refer to dissolution of M_3C_x or M_3N_x . Following the equation $\log_{10}(\text{C}_\text{M}^\text{M} \text{C}_\text{N}^\text{N}) = A - B/T$ with concentrations measured in wt-% and T in K.

the average hardness in the fusion zone is 219 HV. This corresponds to an ultimate tensile strength (UTS) of 738 MPa (107 ksi) according to standard charts for converting hardness to UTS (Ref. 35). This UTS is very close to the UTS of 703 MPa (102 ksi) measured in the tensile testing of the high-Al weld specimen after PWHT. For the low-Al weld, the average hardness in the fusion zone is 247 HV, which corresponds to a UTS of 841 MPa (122 ksi) according to the conversion table. The room-temperature strength of the high-Al weld (738 MPa) is only somewhat (12%) lower than that of the low-Al weld (841 MPa). As suggested by one reviewer of the present study,

Fig. 2 was replotted such that the applied stress was substituted by the ratio of the applied stress to the UTS. The two curves only moved slightly closer to each other instead of collapsing onto one. This new plot seems to suggest that the much lower creep resistance of the high-Al weld was not caused by its lower strength but by its less favorable microstructure (including its coarse precipitates).

Optical Microscopy and -Ferrite

The optical microstructure of the high-Al weld is shown in Fig. 7. The presence of δ -ferrite in the fusion zone

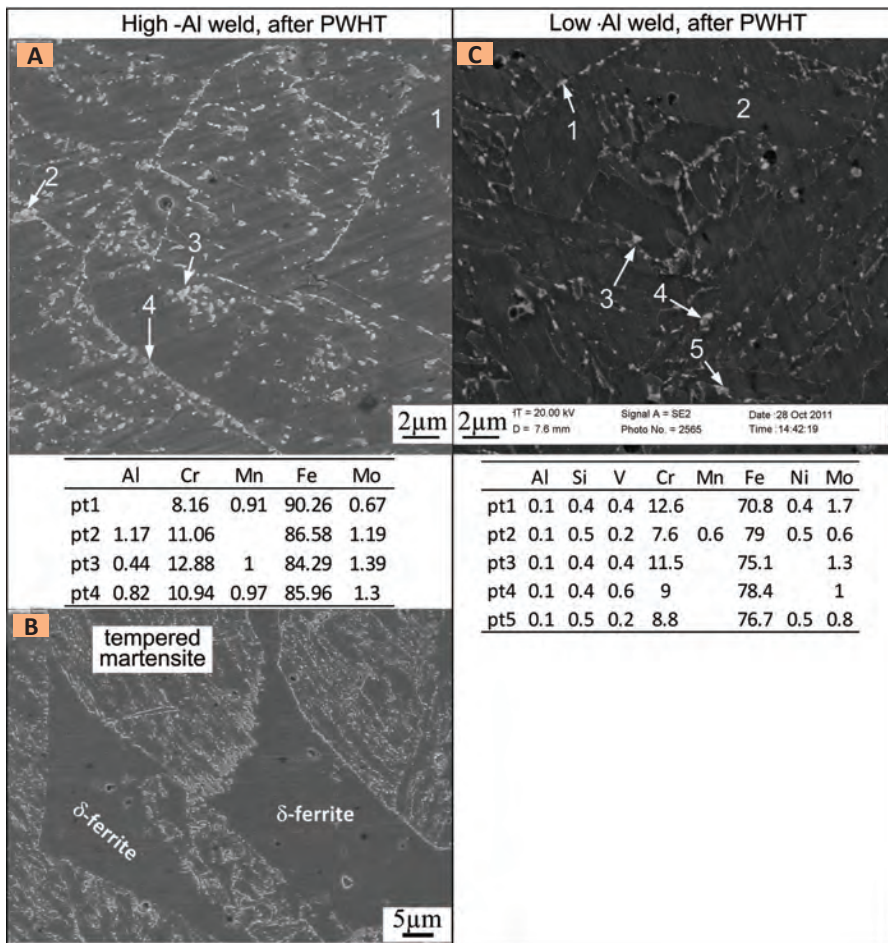


Fig. 10 — Results of EDS composition analysis after postweld heat treatment. A — High-Al weld in area free of δ -ferrite; B — δ -ferrite in high-Al weld showing no precipitates; C — low-Al weld. Cr contents are higher at precipitates 2, 3, 4 than matrix at point 1 in A and at precipitates 1 and 3 than matrix at point 2 in C, suggesting the precipitates are likely to be $M_{23}C_6$.

is evident. A polygonal, light-etching phase distinctly different from the surrounding martensite matrix can be seen in the HAZ of the second to last pass (Fig. 7B) and the HAZ of the last pass (Fig. 7C). This phase is expected to be δ -ferrite, judging from its significantly lower hardness than the surrounding matrix. Although the weld metal can be reheated into the δ + γ region of the phase diagram during multipass welding, the presence of δ -ferrite is not likely to be caused by this reheating. First, reheating also occurred in the low-Al weld made by multipass SMAW but, as is shown subsequently, no δ -ferrite was found. Second, δ -ferrite was found in the fusion zone of the last pass of the high-Al weld (Fig. 7D), which was not reheated by any passes.

The presence of δ -ferrite suggests it

did not transform completely to austenite during cooling. For the purpose of discussion, the quasi-binary phase diagram calculated for T91 steel (reasonably close to P91 steel) by Ayala et al. (Ref. 36) using *Thermo-Calc* is shown in Fig. 8. The carbon contents of the high- and low-Al welds are 0.114 and 0.117 wt-%, respectively (Table 2). As shown, the weld pool solidifies with δ -ferrite as the primary solidification phase. δ -ferrite transforms to austenite, which can in turn transform to martensite upon further cooling. However, using in-situ X-ray diffraction by synchrotron radiation, Mayr et al. (Ref. 23) showed that the δ \rightarrow γ transformation in a 9-Cr steel similar to P91 steel is incomplete. With a simulated thermal cycle like in welding, the steel was heated to a peak temperature of 1300°C in the δ + γ

region and cooled to the room temperature. The transformation of δ -ferrite into austenite during cooling was incomplete. About 2% retained δ -ferrite was found in a matrix of martensite.

According to Paul et al. (Ref. 37), the Cr equivalent Cr_{eq} can be written as follows for welds of P91 steel:

$$Cr_{eq} = Cr + 6Si + 4Mo + 1.5W + 11V + 5Nb + 12Al + 8Ti - 40C - 2Mn - 4Ni - 2Co - 30N - Cu \quad (2)$$

where the elements are expressed in wt-%, e.g., 8.09 for Cr, whose content in the high-Al weld is 8.09 wt-%. The plus signs are for elements that are ferrite stabilizers, and the minus signs for those that are austenite stabilizers. As shown, Al is a stronger ferrite stabilizer, 12 times stronger than Cr.

Based on the composition of the high-Al weld shown in Table 2 and Equation 2, the Cr equivalent of the high-Al weld is 11.11. According to Paul et al. (Ref. 37), if the Cr equivalent of the P91 steel is greater than 9, δ -ferrite can exist. This seems to be consistent with the presence of δ -ferrite in the high-Al weld. As for the low-Al weld, the Cr equivalent is 8.25 based on its composition in Table 2 and Equation 2. This is consistent with the microstructure of the low-Al weld in Fig. 9, which shows no δ -ferrite in the matrix.

Electron Microscopy and Precipitates

Figure 10A shows a SEM image, along with the results of EDS composition analysis, of the high-Al weld after PWHT in an area away from δ -ferrite. Here precipitates are visible both along grain boundaries and inside grains. Point 1 represents a location in the matrix away from precipitates. It shows 8.16 wt-% Cr and 0.67 wt-% Mo. The precipitate near point 2 is richer in Cr than point 1, which suggests the precipitate is likely $M_{23}C_6$. Precipitates of $M_{23}C_6$ have been observed in P91 steels (Refs. 1–4). A similar difference has been reported previously. For instance, Panait et al. (Ref. 4) showed a higher Cr content in $M_{23}C_6$ precipitates than in the surrounding matrix. Figure 10B is a similar SEM image in an area with δ -

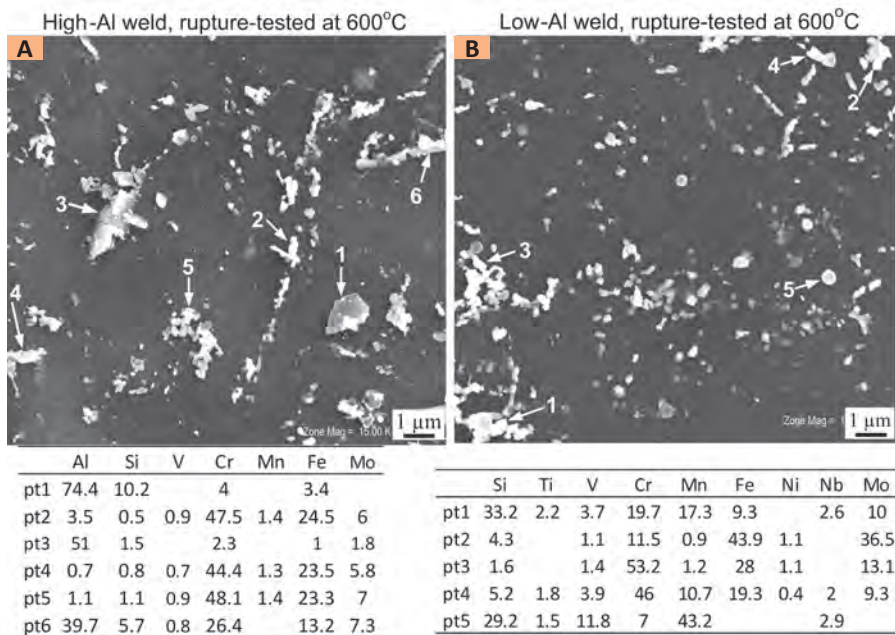


Fig. 11 — SEM images of carbon replicas from transverse cross sections near fracture surfaces of creep specimens tested at 600°C. A — High-Al weld showing coarser precipitates containing Al (points 1, 3); B — low-Al weld showing no such precipitates.

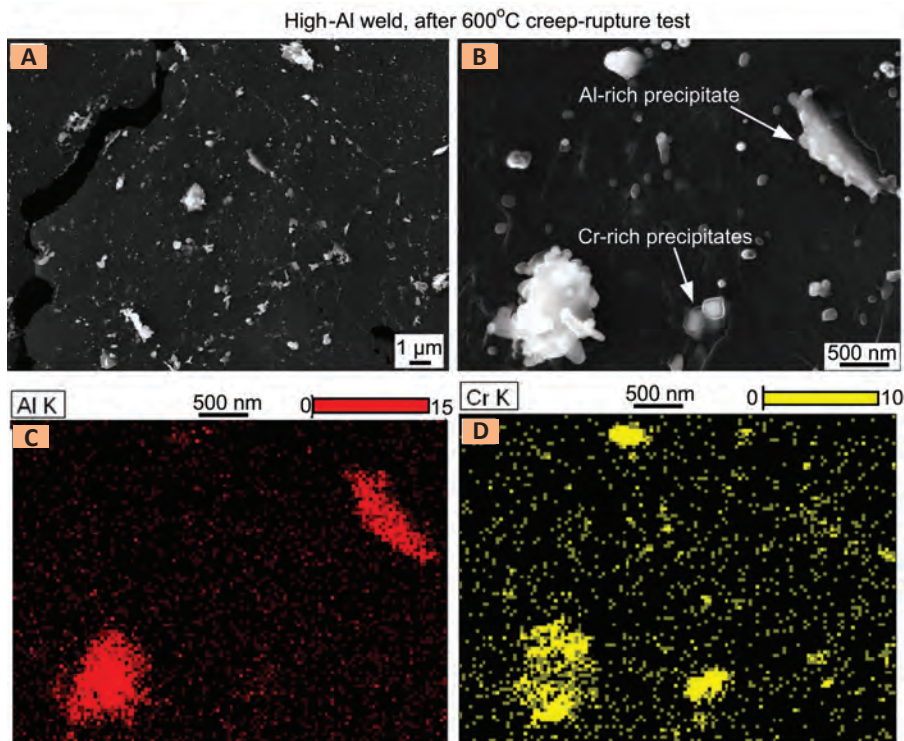


Fig. 12 — Carbon replica from transverse cross section near fracture surface of high-Al weld specimen after 600°C creep rupture test. A — SEM image; B — enlarged SEM image; C — Al distribution in Fig. 12B suggesting presence of coarse Al-rich precipitates; D — Cr distribution in Fig. 12B suggesting presence of Cr-rich $M_{23}C_6$ precipitates.

ferrite. As shown, δ -ferrite is precipitation free, which makes it soft. Figure

10C shows a SEM image of the low-Al weld after PWHT along with the re-

sults of EDS composition analysis. The higher Cr contents of the precipitates near points 1 and 3 than that at point 2 in the matrix suggest that the precipitates are likely $M_{23}C_6$.

Figure 11A shows the SEM image of a carbon replica from the transverse cross section near the fracture surface of the high-Al weld specimen tested at 600°C (1112°F) and 155 MPa. It shows near points 1 and 3 plate-like precipitates that are considerably larger in size than $M_{23}C_6$. The EDS composition analysis shows these precipitates are Al-rich without detectable V. Figure 11B shows the SEM image of a carbon replica from the transverse cross section near the fracture surface of the low-Al weld specimen after creep rupture testing at 600°C and 155 MPa. As compared to the high-Al weld (Fig. 11A), the precipitates are smaller and more uniformly distributed. Furthermore, unlike in the high-Al weld, the precipitates here contain significantly more V and no detectable Al.

Figure 12 shows the element mapping of the transverse cross section near the fracture surface of the high-Al weld specimen tested at 600°C and 155 MPa. Two large precipitates about 1 μ m in size are visible in Fig. 12B, the one in the upper-right corner being plate-like. Both are rich in Al as shown by the Al map in Fig. 12C. The Cr map in Fig. 12D shows two isolated Cr-rich precipitates and two others in the lower left corner that seem to be sitting on top of a large Al-rich precipitate that is presumably plate-like. The two large precipitates in Fig. 12B are further analyzed by transmission electron microscopy (TEM) in Fig. 13. Considering the small but significant N content in the fusion zone, the two large Al-rich precipitates are likely to be AlN. They can be seen in the TEM image in Fig. 13B. The large precipitate on the upper-right corner shows a diffraction pattern similar to that of AlN, as can be seen by comparing Fig. 13C with Fig. 13D.

Figure 14 shows the element mapping of the transverse cross section near the fracture surface of the low-Al weld specimen tested at 600°C and 155 MPa. Precipitates are shown by the SEM image in Fig. 14A, wherein some small precipitates about 100 nm in size are visible. The Cr-map in Fig. 14B suggests these precipitates are $M_{23}C_6$. However,

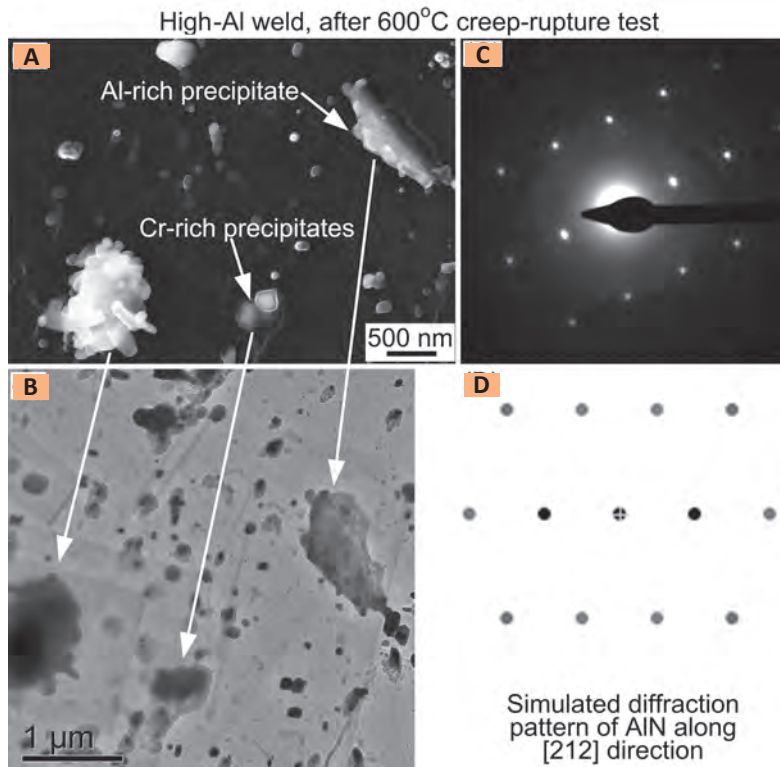


Fig. 13 — Evidence of AlN precipitates in high-Al weld specimen after 600°C creep rupture test: A — SEM image of carbon replica (same as Fig. 12B); B — TEM image at same location as in Fig. 13A; C — electron diffraction pattern of the Al-rich precipitate in Fig. 13A; D — simulated diffraction pattern of AlN indicating the Al-rich precipitate is AlN.

Table 5 — Supersaturation temperature of Nitrides in High-Al Weld

| Compound | A | B | Supersaturation temperature (°C) |
|----------|----------------|-------|----------------------------------|
| VN | 2.27 | 7070 | 1257 |
| VN | 3.46 + 0.12%Mn | 8330 | 1175 |
| AlN | 1.80 | 7750 | 1477 |
| AlN | 1.03 | 6770 | >1500 |
| NbN | 4.04 | 10230 | 1087 |
| NbN | 3.70 | 10800 | 1231 |

Table 6 — Supersaturation temperature of Nitrides in Low-Al Weld

| Compound | A | B | Supersaturation temperature (°C) |
|----------|----------------|-------|----------------------------------|
| VN | 2.27 | 7070 | 1257 |
| VN | 3.46 + 0.12%Mn | 8330 | 1319 |
| AlN | 1.80 | 7750 | <800 |
| AlN | 1.03 | 6770 | <800 |
| NbN | 4.04 | 10230 | 1101 |
| NbN | 3.70 | 10800 | 1247 |

the coexistence of more than one type of precipitate seems visible at some locations in the SEM image Fig. 14A. The V-map in Fig. 14C suggests the presence of V-containing precipitates and their coexistence with the larger $M_{23}C_6$ precipitates. These V-containing precipitates are likely to be V(CN).

Thermodynamic and Kinetic Analyses

A thermodynamic analysis of nitride precipitates can be made based on the Ellingham diagram of nitrides shown in Fig. 15A (Ref. 38) for the relative stabi-

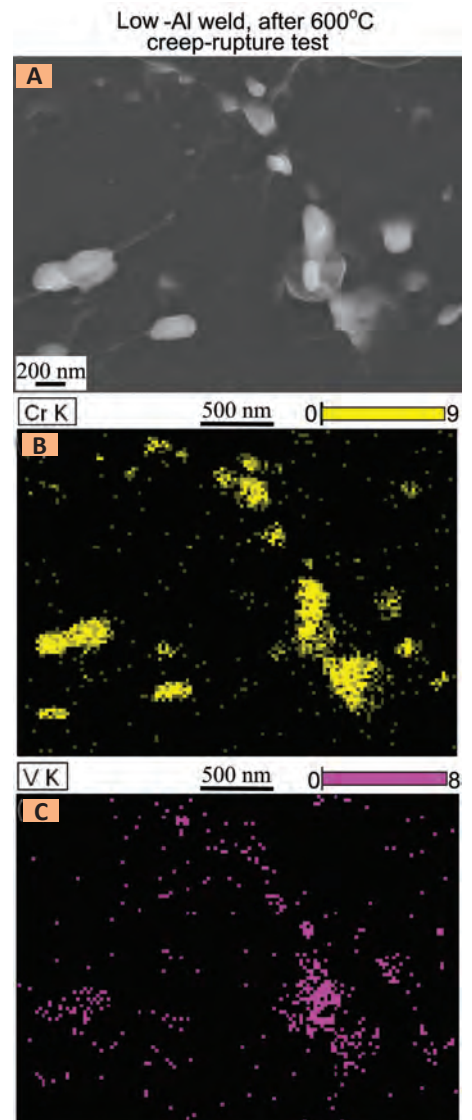


Fig. 14 — Evidence of V(CN) precipitates in low-Al weld specimen after 600°C creep rupture test: A — SEM image of carbon replica from transverse cross section near fracture surface; B — Cr distribution suggesting presence of Cr-rich $M_{23}C_6$ precipitates; C — V distribution suggesting presence of V(CN) precipitates.

ty of AlN, VN, and NbN. Since a nitride with a lower free energy of formation has a greater tendency to form, the diagram shows a greater tendency for AlN to form than either VN or NbN. This is consistent with the presence of AlN precipitates in the high-Al weld. However, the Ellingham diagram shows the standard-state condition and does not consider the actual concentrations of Al, V, Nb, and N in the welds.

A kinetic analysis of nitride precipi-

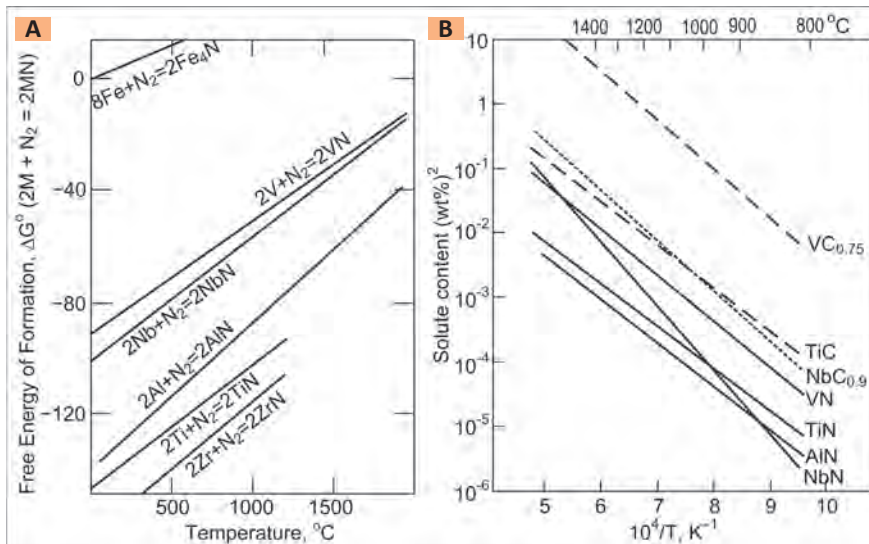


Fig. 15 — Effect of temperature on formation of nitrides. A — Ellingham diagram showing a greater tendency for AlN to form than VN and NbN under standard state (Ref. 38); B — solubility products of some nitrides and carbides in austenite (Ref. 39).

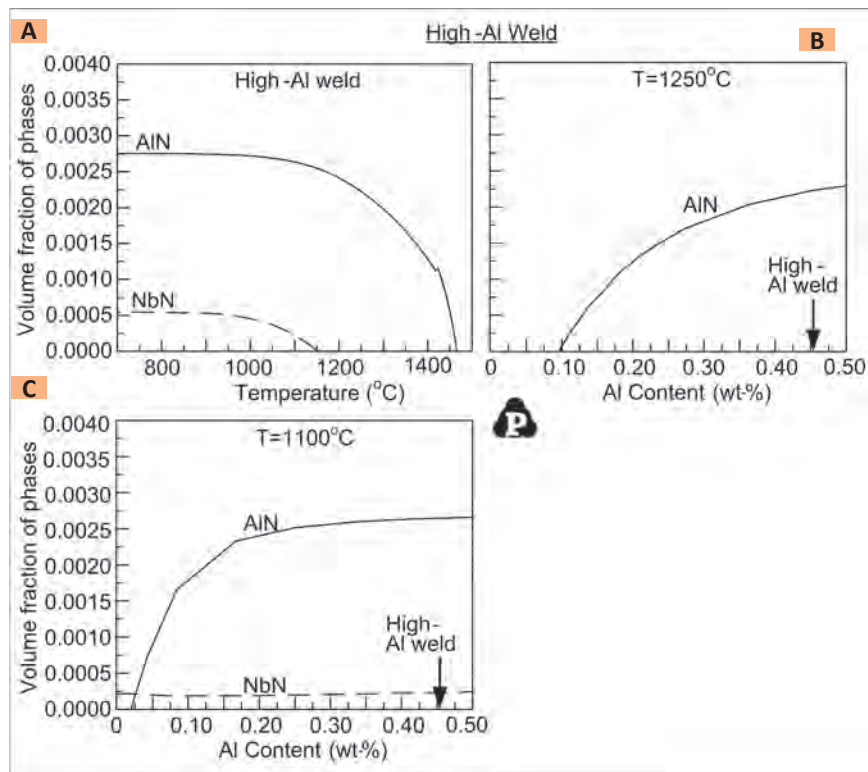


Fig. 16 — Dominance of AlN over NbN (and VN, which does not even form) in high-Al weld (0.455 wt-% Al). A — Volume fractions of nitrides vs. temperature; B — volume fractions of nitrides vs. Al content at 1250°C (with Al replacing Fe while contents of other alloy elements being kept identical to Table 2); C — volume fractions of nitrides vs. Al content at 1100°C. All curves calculated using Pandat (Ref. 42) and Paniron (Ref. 43) of CompuTherm.

tates can be made based on the solubility products of nitrides. Figure 15B shows the solubility products of nitrides (and some carbides) in steel ac-

cording to Aronsson (Ref. 39). The solubility products of all the nitrides decrease as the temperature decreases. AlN has the lowest solubility product

at the temperature above 863°C ($10^4/1136 \text{ K} = 8.8 \text{ K}^{-1}$), indicating AlN is likely to precipitate first during cooling after solidification. For a metal M, the solubility product of its nitride MN can also be calculated using the following equation (Ref. 40):

$$\log_{10}(C_M C_N) = A - B/T \quad (3)$$

where the concentration C is in wt-% and temperature T in degrees Kelvin. The constants A and B are given in Table 4 in two different sets of values according to Ashby and Easterling (Ref. 40).

For a MN nitride such as AlN, VN, and NbN, the level of supersaturation at a given temperature can be defined as follows:

$$\begin{aligned} \text{Level of supersaturation} = \\ (\text{wt-\% of } M \text{ in weld}) \times (\text{wt-\% of N in weld}) / \\ (C_M C_N) \end{aligned} \quad (4)$$

where the wt-% of M in the weld and the wt-% of N in the weld are given in Table 2 (composition of welds). A precipitate is considered supersaturated when the ratio is greater than 1.0, and the higher the ratio is, the greater the tendency for the precipitate to form. Calculated results for the high-Al weld based on Equations 3 and 4 in Table 2 are summarized in Table 5. As shown, AlN can reach supersaturation upon cooling to 1477°C or even before 1500°C. However, NbN and VN cannot reach supersaturation until further cooling to lower temperatures: NbN to 1087° or 1231°C, and VN to 1175° or 1257°C. Consequently, during cooling AlN can precipitate before VN and NbN, and this is consistent with the fact that no V-rich precipitates were found in the high-Al weld. Thus, AlN precipitates could have formed at the expense of V(CN) and Nb(CN) precipitates. Therefore, the absence of creep-resistant V(CN) and Nb(CN) precipitates is consistent with the poor creep resistance of the high-Al weld. It is worth mentioning that AlN inclusions about 1 μm in size were found in FCAW deposits containing 1.70 wt-% Al and 0.064 wt-% N without V or Nb, and they exhibited a faceted morphology (Ref. 41).

Calculated results for the low-Al weld based on Equations 3 and 4 and

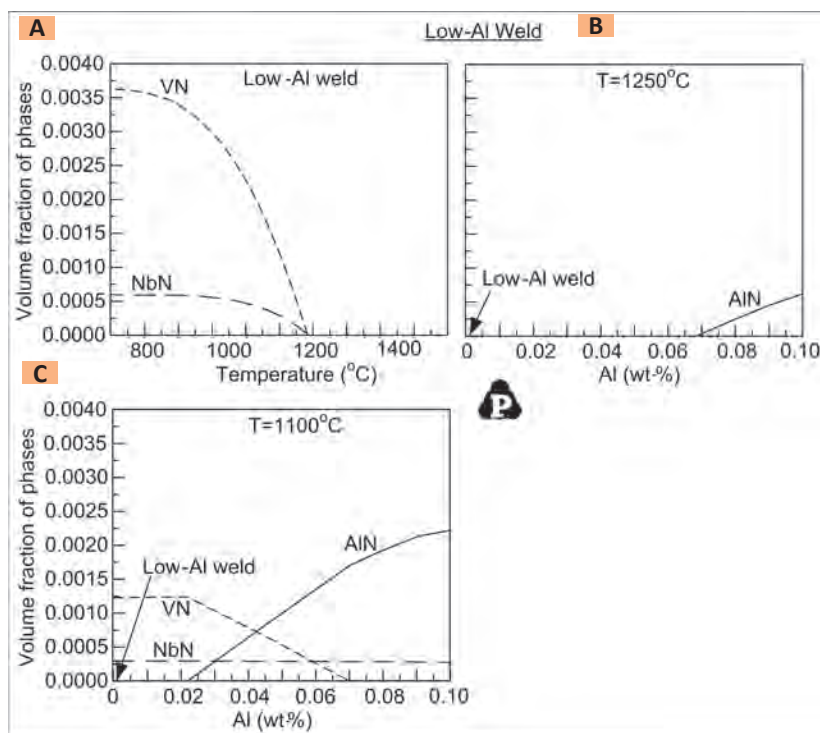


Fig. 17 — Dominance of VN and NbN over AlN in low-Al weld (0.001 wt-% Al).
A — Volume fractions of nitrides vs. temperature; B — volume fractions of nitrides vs. Al content at 1250°C; C — volume fractions of nitrides vs. Al content at 1100°C. All curves calculated using Pandat (Ref. 42) and PanIron (Ref. 43) of CompuTherm.

Table 2 are summarized in Table 6. The lack of AlN in the low-Al weld is less due to the competition with other nitrides as the fact that there is almost no Al in the weld. Because of the very low Al content, AlN does not reach supersaturation upon cooling until below 800°C. However, NbN and VN can reach supersaturation upon cooling to higher temperatures: NbN to 1101° or 1247°C, and VN to 1257° or 1319°C. Consequently, during cooling VN and NbN can precipitate before AlN, and this is consistent with the fact that no Al-rich precipitates could be found in the low-Al weld.

In the study of Quintana et al. (Ref. 41) on Fe-C-Al-Mn steel welds made by FCAW, the thermodynamics computer software *ThermoCalc* was used to analyze the formation of AlN, Al₂O₃, and Ti(CN) precipitates in the welds.

In the present study, the thermodynamic computer software *Pandat* (Ref. 42) and the database *PanIron* (Ref. 43) of CompuTherm, LLC, were used to calculate the formation of nitride in the welds based on their compositions in Table 2. The calculated results for the high-Al weld are shown in Fig. 16.

Figure 16A shows that AlN precipitation starts at a much higher temperature than NbN formation and that no VN precipitates during cooling. Figure 16B and C showed volume fractions of nitrides vs. the Al content at 1250° and 1100°C, respectively. It shows that at 0.45 wt-% Al, precipitation of AlN dominates that of NbN and precipitation of VN does not even occur, consistent with the experimental results. It is perhaps worth mentioning that the solubility of nitrogen is much higher in δ -ferrite than in γ -ferrite (Ref. 44). This may suggest that some N may be trapped in δ -ferrite in the case of the high-Al weld, thus further reducing the amount of N available for the precipitation of NbN and VN.

Similar results calculated for the low-Al weld are shown in Fig. 17. Figure 17C shows that at 0.001 wt-% Al, only VN and NbN can precipitate out but not the AlN, which is consistent with the experimental results. The lack of AlN in the low-Al weld is less due to the competition with other nitrides as the fact that there is almost no Al in the weld.

Conclusions

1) Stress rupture tests of welds of P91 steel made with significantly different Al contents in the fusion zones have shown that increasing the Al content can significantly reduce the creep resistance of P91 steel welds, from up to about 5000 h at 0.001 wt-% Al to up to about 300 h at 0.455 wt-% Al under the tested conditions in the present study.

2) Optical microscopy of the welds has shown that increasing the Al content can promote the formation of retained δ -ferrite in the matrix of tempered martensite, which is detrimental to the creep resistance of P91 steel. This effect of Al on the δ -ferrite formation is consistent with Al being a powerful ferrite stabilizer, twelve times more powerful than Cr according to Equation 2.

3) Electron microscopy and EDS composition analysis of the welds have shown that increasing the Al content can promote the formation of coarse (about 1 μ m) AlN precipitates at the expense of the fine (< 100 nm) VN precipitates needed to resist creep.

4) Thermodynamic analysis based on the Ellingham diagram of nitrides suggests that AlN can have a greater tendency to precipitate than VN and NbN, at least under the standard state.

5) Kinetic analysis based on the solubility products of nitrides and the composition of the high-Al weld suggests that, during cooling after solidification, supersaturation can be reached to cause precipitation at a significantly higher temperature for AlN than for NbN and VN. Thus, AlN can be expected to precipitate first and use up N before NbN and VN can precipitate.

6) Computations using the computer software *Pandat* suggest that the dominance of AlN precipitation in the high Al-weld and the absence of AlN formation in the low-Al weld.

7) The presence of retained δ -ferrite and the absence of VN (or V(CN)) and NbN (or Nb(CN)) precipitates have contributed to the much lower creep resistance of the high-Al weld.

Acknowledgments

This work was supported by Hobart Brothers Co., Troy, Ohio, and the Na-

tional Science Foundation under Grant No. IIP-1034695 through the Industry/University Collaborative Research Center (I/UCRC) for Integrated Materials Joining Science for Energy Applications. The authors would like to thank Ms. Soumya Mohan of the Department of Materials Science and Engineering at The Ohio State University for her assistance in some of the hardness measurements across the welds. They would also like to thank Prof. John H. Perepezko of the Department of Materials Science and Engineering at the University of Wisconsin-Madison for helpful discussions on the kinetic analysis.

References

- Ennis, P. J., and Filemonowicz, A. C. 2003. Recent advances in creep resistant steels for power plant applications. *Sadhana* 28: 709–730.
- Hald, J. 2008. Microstructure and long-term creep properties of 9–12% Cr steels. *International Journal of Pressure Vessels and Piping* 85: 30–37.
- Falat, L., Vyrostkava, A., Homolova, V., and Svoboda, M. 2009. Creep deformation failure of E911/E911 and P92/P92 similar weld-joints. *Engineering Failure Analysis* 16: 2114–2120.
- Panaït, C. G., Bendick, W., Fuchsmann, A., Gourgues-Lorenzon, A. F., and Besson, J. 2010. Study of the microstructure of the Grade 91 steel after more than 100,000 h of creep exposure at 600°C. *International Journal of Pressure Vessels and Piping* 87: 326–335.
- Rojas, D., Garcia, J., Prat, O., Sauthoff, G., and Kaysser-Pyzalla, A. R. 2011. 9% Cr heat resistant steels. Alloy design, microstructure evolution and creep response at 650°C. *Materials Science and Engineering A* 528: 5164–5176.
- Arivazhagan, B., Sundaresan, S., and Kamaraj, M. 2009. A study on influence of shielding gas composition on toughness of flux-cored arc weld of modified 9Cr–1Mo (P91) steel. *Journal of Materials Processing Technology* 209: 5245–5253.
- Siresha, M., Albert, S. K., and Sundaresan, S. 2001. Microstructure and mechanical properties of weld fusion zones in modified 9Cr1Mo steel. *Journal of Materials Engineering and Performance* 10(3): 320–330.
- Bhadeshia, J. A., Mazur, W., and Bhadeshia, H. K. D. H. 2006. Type IV cracking in ferritic power plant steels. *Materials Science and Technology* 22: 1387–1395.
- David, S. A., Siefert, J. A., and Feng, Z. 2013. Welding and weldability of candidate ferritic alloys for future advanced ultrasupercritical fossil power plants. *Science and Technology of Welding and Joining* 18: 631–651.
- Sawada, K., Hongo, H., Watanabe, T., and Tabuchi, M. 2010. Analysis of the microstructure near the crack tip of ASME Gr. 92 steel after creep crack growth. *Materials Characterization* 61: 1097–1102.
- Blum, W., and Eisenlohr, P. 2009. Dislocation mechanics of creep. *Materials Science and Engineering A* 510–511: 7–13.
- Helisa, L., Toda, Y., Hara, T., and Miyazaki, H. 2009. Effect of cobalt on the microstructure of tempered martensitic 9Cr steel for ultra-supercritical power plants. *Materials Science and Engineering A* 510–511: 88–94.
- Abe, F., Taneike, M., and Sawada, K. 2007. Alloy design of creep resistant 9Cr steel using a dispersion of nano-sized carbonitrides. *International Journal of Pressure Vessels and Piping* 84: 3–12.
- Abe, F. 2008. Precipitate design for creep strengthening of 9% Cr tempered martensitic steel for ultra-supercritical power plants. *Science and Technology of Advanced Materials* 9: 1–15.
- Klotz, U. E., Solenthaler, C., and Uggowitzer, P. J. 2008. Martensitic-austenitic 9–12% Cr steels — Alloy design, microstructural stability and mechanical properties. *Materials Science and Engineering A* 476: 186–194.
- Sawada, K., Bauer, M., Kauffmann, F., Mayr, P., and Klenk, A. 2010. Microstructural change of 9% Cr-welded joints after long-term creep. *Materials Science and Engineering A* 527: 1417–1426.
- Shen, Y. Z., Kim, S. H., Cho, H. D., Han, C. H., and Ryu, W. S. 2009. Precipitate phases of a ferritic/martensitic 9% Cr steel for nuclear power reactors. *Nuclear Engineering and Design* 239: 648–654.
- Siefert, J. A., and David, S. A. 2014. Weldability and weld performance of candidate austenitic alloys for advanced ultrasupercritical fossil power plants. *Science and Technology of Welding and Joining* 19: 271–294.
- Das, C. R., Albert, S. K., Bhaduri, A. K., Srinivasan, G., and Murty, B. S. 2008. Effect of prior microstructure on microstructure and mechanical properties of modified 9Cr–1Mo steel weld joints. *Materials Science and Engineering A* 477: 185–192.
- Yu, X., Babu, S. S., Terasaki, H., Komizo, Y., Yamamoto, Y., and Santella, M. L. 2013. Correlation of precipitate stability to increased creep resistance of Cr-Mo steel welds. *Acta Materialia* 61: 2194–2206.
- Abson, D. J., and Rothwell, J. S. 2013. Review of type IV cracking of weldments in 9–12%Cr creep strength enhanced ferritic steels. *International Materials Reviews* 58: 437–473.
- Babu, S. S., Elmer, J. W., Vitek, J. M., and David, S. A. 2002. Time-resolved X-ray diffraction investigation of primary weld solidification in Fe-C-Al-Mn steel welds. *Acta Materialia* 50: 4763–4781.
- Mayr, P., Palmer, T. A., Elmer, J. W., Specht, E. D., and Allen, S. M. 2010. Formation of delta ferrite in 9 wt.% Cr steel investigated by in-situ X-ray diffraction using synchrotron radiation. *Metallurgical and Materials Transactions A* 41(10): 2462–2465.
- Arivazhagan, B., Srinivasan, G., Albert, S. K., and Bhaduri, A. K. 2011. A study on influence of heat input variation on microstructure of reduced activation ferritic martensitic steel weld metal produced by GTAW process. *Fusion Engineering and Design* 86: 192–197.
- Onoro, J. 2006. Martensite microstructure of 9–12%Cr steels weld metals. *Journal of Materials Processing Technology* 180: 137–142.
- Naoi, H., Ohgami, M., Liu, X., and Fujita, T. 1997. Effects of aluminum content on the mechanical properties of a 9Cr–0.5Mo–1.8W steel. *Metallurgical and Materials Transactions A* 28: 1195–1203.
- Magnusson, H., and Sandstrom, R. 2009. Influence of aluminium on creep strength of 9–12% Cr steels. *Materials Science and Engineering A* 527: 118–125.
- Kou, S. 2003. *Welding Metallurgy*, Second edition, John Wiley and Sons. 66–75.
- Vaillant, J. C., Vandenberghe, B., Hahn, B., Heuser, H., and Jochum, C. 2008. T/P23, 24, 911 and 92: New grades for advanced coal-fired power plants — Properties and experience. *International Journal of Pressure Vessels and Piping* 85: 38–46.
- AWS A5.29/A5.29M:2010, *Specification for Low-Alloy Steel Electrodes for Flux Cored Arc Welding*. American Welding Society, Miami, Fla.
- Silwal, B., Li, L., Deceuster, A., and Griffiths, B. 2013. Effect of postweld heat treatment on the toughness of heat-affected zone for grade 91 steel. *Welding Journal* 92(4): 80-s to 87-s.
- Hanhold, B., Babu, S. S., and Cola, G. 2013. Investigation of heat affected zone softening in armor steels — Part 2: Mechanical and microstructural heterogeneity. *Science and Technology of Welding & Joining* 18: 253–260.
- Yaghi, A. H., Hyde, T. H., Becker, A. A., and Sun, W. 2008. Finite element simulation of welding and residual stresses in a P91 steel pipe incorporating solid-state

phase transformation and post-weld heat treatment. *Journal of Strain Analysis for Engineering Design* 43: 275–293.

34. Reed, R., and Bhadeshia, H. K. D. H. 1994. A model for multipass steel welds. *Acta Metallurgica et Materialia* 42: 3663–3678.

35. The hardness-UTS conversion table at www.mwsco.com/kb/articles/19990630e.html.

36. Ayala, E., Roman, M., Vega, J., Gomez, X., Genez-Acebo, T., and Echberria, J. 1999. Delta ferrite formation in 9–12% chromium steel weldments. *Advanced Heat Resistant Steels for Power Generation*: 633–643.

37. Paul, T. V., Saroja, S., Hariharan, P., Rajadurai, A., and Vijayalakshmi, M.

2007. Identification of microstructural zones and thermal cycles in a weldment of modified 9Cr-1Mo steel. *J Mater Sci* 42: 5700–5713.

38. Mashhadi, H. A., Kennedy, G., Tanaka, S., and Hokamoto, K. 2011. Effect of aluminum content on the mechanochemical synthesis of in-situ TiN in the Al-Ti-AlN system and subsequent shock consolidation. *Physica B* 406: 1211–1221.

39. Aronsson, B. 1969. *Steel-Strengthening Mechanisms*. 77–87.

40. Ashby, M. F., and Easterling, K. E., 1982. A first report on diagrams of grain growth in welds. *Acta Metallurgica* 30: 1969–1978.

41. Quintana, M. A., McLane, J., Babu,

S. S., and David, S. A. 2001. Inclusion formation in self shielded flux-cored arc welds. *Welding Journal* 80: 98-s to 105-s.

42. Pandat. 2001. Phase diagram calculation software package for multicomponent systems. CompuTherm, LLC, Madison, Wis.

43. PanIron. 2001. Thermodynamic database for iron-based alloys. CompuTherm, LLC, Madison, Wis.

44. *The Making, Shaping and Treating of Steel*, 10th edition. 1985. edited by W. T. Lankford Jr., N. L. Samways, R. F. Craven, and H. E. McGannon, Association of Iron and Steel Engineers, Pittsburgh, Pa., p. 405.

Bring Brand Awareness to Your Company

By Placing Your Product Video on the AWS Website

For more information visit our website at <http://videos.aws.org> or please contact:

Lea Paneca
lea@aws.org
(800) 443-9353, ext. 220

Sandra Jorgensen
sjorgensen@aws.org
(800) 443-9353, ext. 254